

## Electron Beam Coherency Determined from Interferograms of Carbon Nanotubes

B. Cho\* and C. Oshima†

Korea Research Institute of Standards and Science, Daejeon 305-340, Korea. \*E-mail: blcho@kriss.re.kr

†Department of Applied Physics, Waseda University, Tokyo 169, Japan

Received December 6, 2012, Accepted December 26, 2012

A field emission projection microscope was constructed to investigate the atomic and chemical-bonding structure of molecules using electron in-line holography. Fringes of carbon nanotube images were found to be interferograms equivalent to those created by the electron biprism in conventional electron microscopy. By exploiting carbon nanotubes as the filament of the electron biprism, we measured the transverse coherence length of the electron beam from tungsten field emitters. The measurements revealed that a partially coherent electron-beam was emitted from a finite area.

**Key Words** : Field emission, Interferogram, Projection microscope, Coherence, Carbon nanotube

### Introduction

Electron interferometry and holography have drawn wide interest because they are expected to yield 3-dimensional information about the atomic and chemical bonding structures of molecules.<sup>1</sup> Electron holography is usually implemented using an electron biprism interferometer placed in a complicated transmission electron microscope. The biprism divides an electron beam (E-Beam) into two mutually coherent beams. For off-axis electron holography, an object is illuminated by one of the two beams. An electron interferogram or hologram is then obtained by overlapping the two beams on a screen.

A field emission (FE) projection microscope (FPM) may be one of the simplest electron microscopes, containing no electron optical elements. It consists of just three components: the FE electron source, the specimen, and the imaging screen. When an object is illuminated by an E-Beam radially propagating from an FE source, its shadow image is projected on the screen with a magnification ratio of  $a+b$  (the distance between the source and the screen) to  $a$  (the distance between the source and the specimen), as shown in

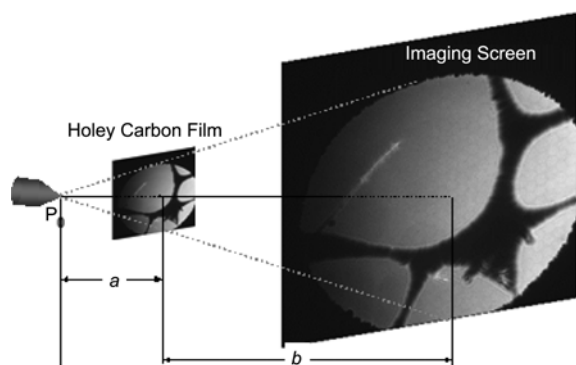


**Figure 1.** Schematic experimental configuration of field emission projection microscope. The distance between the field emission tip and the Holey carbon film, and that between the holey carbon film and the screen are denoted by  $a$  and  $b$ , respectively.

Figure 1. If a molecular object partly transparent to electrons is illuminated by a coherent E-Beam, its in-line hologram appears on the screen as shown in Figure 2.

The field emission electron source has been a main driving force behind the development of modern high-resolution electron microscopy and interferometry because of its inherent high coherency and brightness.<sup>2</sup> It has a small spatial size of  $\sim 50$  nm and a narrow energy width of  $\sim 0.3$  eV; the former directly relates to the spatial coherence and the latter to the temporal coherence. FE-sources have usually been treated as incoherent sources despite the finite coherence length of the electrons inside the solid.<sup>3</sup> The high degree of coherence at specimens in electron microscopy has been ascribed to the high brightness of FE guns; the plausible relation between the coherence of a field-emitted electron beam and the coherence of electrons inside solids has been ignored.

The coherence of an E-Beam can be evaluated with interferograms, *i.e.* interference patterns.<sup>4</sup> According to coherence theory, the visibility of interferograms improves with the enhancement of the coherency of the E-Beam.<sup>5</sup> In this regard, FPM is a promising tool for evaluating the coherency of an E-Beam because it is one of the simplest methods to present

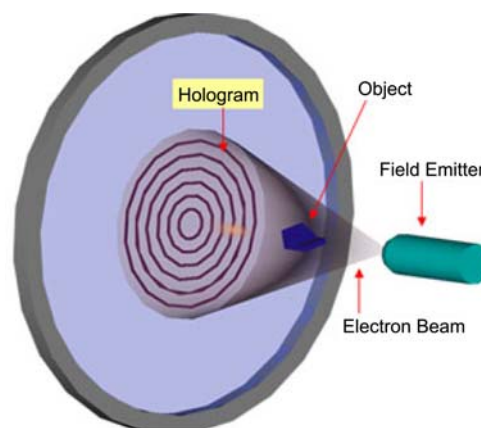


**Figure 2.** Schematic configuration of electron in-line holography experiment.

electron interferograms.<sup>6</sup> Actually, the transverse coherence length (TCL) of E-Beams from various field emitters has been measured using Fresnel edge fringe patterns at the edge of carbon films in FPM images.<sup>7-9</sup> However, the visibility of Fresnel edge fringes depends on the straightness of the edge and its thickness,<sup>10</sup> which cannot be determined in the FPM.

By employing highly coherent FE sources in our low-temperature FPM, we have been able to take some of the best quality interference or diffraction images.<sup>11,12</sup> We present here various interferograms of carbon nanotubes and report the results of evaluating the coherency of E-Beams and FE sources using the interferograms. A preliminary account of some early results has been given in the previous letter;<sup>11</sup> the present paper gives a full description of the coherence evaluation process. Although the explanations for some parts of the present work remain tentative at best, we consider the results to be sufficiently interesting to deserve publication at this stage.

### Experimental

The experiment was conducted in our low-temperature FPM. The experimental apparatus and procedure are described elsewhere in detail.<sup>12</sup> In brief, a holey carbon film was employed as the extractor electrode. Electrochemically etched polycrystalline tungsten tips were used as the FE source. FE sources were cleaned using an E-Beam heater and loaded onto the tip holder carried by a piezo tube. Except for small holes for E-Beam passage, the whole FE unit is completely shrouded by permalloy for magnetic shielding. A microchannel plate (MCP) was used for the imaging screen. Figure 3 provides a schematic illustration of our FPM.

The loadlock, preparation chamber, and control electronics are based on standard commercial designs (JEOL). The main chamber is connected to the preparation chamber through an all-metal gate valve. Both chambers are equipped with a sputter ion pump and a titanium sublimation pump. The base pressures in the preparation and main chamber are below  $2 \times 10^{-8}$  Pa and below  $3.0 \times 10^{-8}$  Pa without cooling,

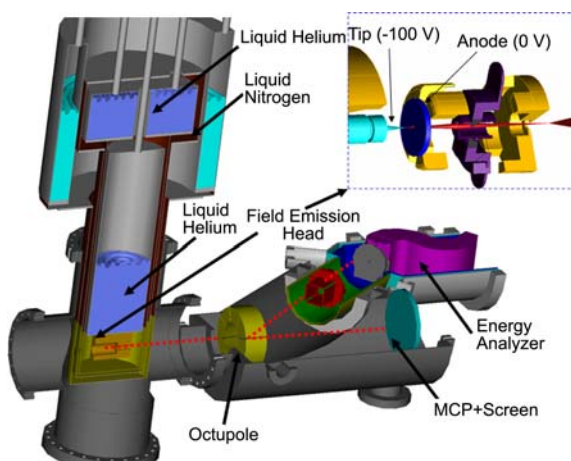


Figure 3. Schematic view of the experimental apparatus.

respectively. A load lock chamber is used to exchange tips and anodes in and out of the UHV environments without venting the entire system to the atmosphere (venting the entire system, baking out, and returning to low temperatures require at least ten days turn-around time). The UHV chambers housing the entire system are isolated from floor vibration by bolting them to an optical tabletop fitted with pneumatic legs.

### Results and Discussion

**Interference and Fresnel Edge Fringe Patterns.** At the initial stage of tip approach, clear FPM images of the holey carbon film showed up on the MCP. With the tip approach, Fresnel edge fringe patterns appeared at the edge of the large holes, as shown in Figure 4(a). Small holes generated patterns similar to Fresnel diffraction patterns displayed in optics textbooks,<sup>5</sup> as shown in Figure 4(b). Given a hole of known diameter, one may evaluate the coherency of the E-Beam by simulating the diffraction patterns of the small hole.

When there are two neighboring holes on a holey carbon film, interference fringes are observed between them, as shown in Figure 4(c). Multiple neighboring holes generated interference spots, as shown in Figure 4(d), which might have been wrongly interpreted as atomic images.<sup>6</sup>

Coherence theory states that the effective size  $r_{\text{eff}}$  of an electron source can be determined from the visibility of the interferograms generated between the holes. The TCL  $\xi_{\text{Ta}}$  of

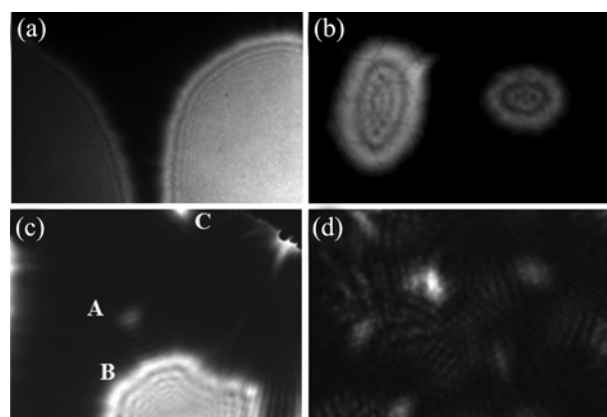


Figure 4. Fresnel edge fringe pattern observed in FPM of relatively large holes (a) and of relatively small holes (b). Interferograms between two holes (c) and among multiple holes (d).

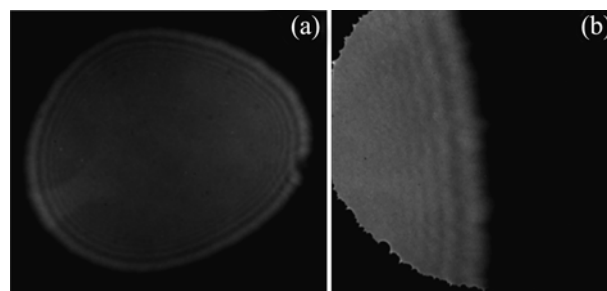


Figure 5. Fresnel edge fringe image at low magnification (a) and at high magnification (b).

an E-Beam on the film is given by the van Cittert-Zernike theorem:<sup>5</sup>

$$\xi_{Ta} = \frac{\lambda \cdot a}{\pi \cdot r_{\text{eff}}} \quad (1)$$

where  $a$  is the distance between the source and the film. As the value of  $\xi_{Ta}$  shortens with tip approach, *i.e.*, decreasing  $a$ , the interferogram between the holes blurs. For  $\xi_{Ta}$  shorter than the spacings of the holes, the interferogram becomes completely invisible. For example, interference fringes were observed between holes A and B but not between holes A and C, as can be seen in Figure 4(c). Knowing the tip-hole distance  $a$  and the hole spacings, thus, one may determine the E-Beam coherency and, consequently, the effective source size. In the present paper, the TCL  $\xi_{Ta}$  is not determined using interference fringes between holes because holes were found only by chance and no information was available on the distance between the holes.

The effective source size  $r_{\text{eff}}$  was estimated using the Fresnel edge fringe method.<sup>7</sup> Figure 5 shows the Fresnel edge fringes at two different magnifications. The width of the band of the Fresnel edge fringes, corresponding to the TCL  $\xi_{Tb}$  on the observation screen, increased with tip approach. The van Cittert-Zernike theorem yielded effective source sizes of approximately 7.5 and 1.5 nm for images shown in Figure 5(a) and (b), respectively. In spite of the use of poly-crystal W tips, those values were close to the effective source sizes of the nanotips or nanotubes as estimated using Fresnel edge fringes.<sup>8,9</sup> In the meantime, if the Fresnel edge fringe method was valid and the source size was constant,  $\xi_{Tb}$  on the screen and, consequently, the effective source size would remain constant regardless of the magnification ratio.

**Nano Electron Biprism.** The electron biprism is one of the most widely used electron interferometers. Missiroli *et al.* gave an excellent introductory description of the electron biprism.<sup>4</sup> Here we give a brief account of the electron biprism, following the notation employed in their paper.

The electron biprism consists of a very thin conducting filament of radius  $r$ , placed between two grounded plates. The incoming E-Beam is divided into two partial beams when passing the filament. If a positive electric potential was applied to the filament, the two beams would be de-

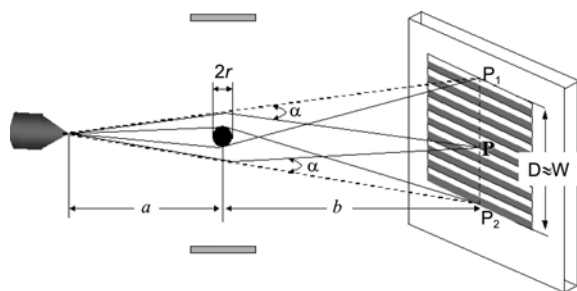


**Figure 6.** Basic parameters of an electron biprism illuminated by an FE tip. The distance between the field emission tip and the biprism, and that between the biprism and the screen, are denoted by  $a$  and  $b$ , respectively. The deflection angle of the electron beam is denoted by  $\alpha$ .

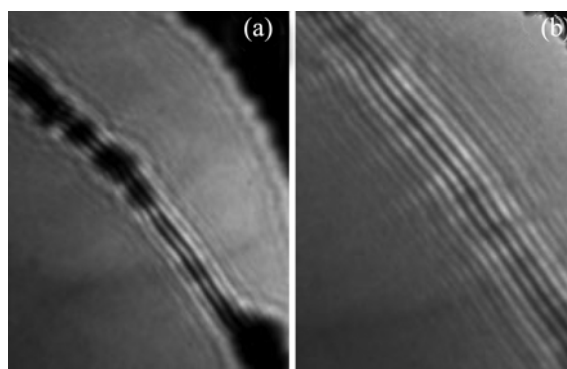


**Figure 7.** Nano biprism interferograms of the first group at low magnification (a) and at high magnification (b).

flected towards the filament through a constant angle and superpose to form straight fringes of uniform spacing  $S$  on the image plane. Figure 6 shows the basic parameters of an electron biprism illuminated by an FE tip. In the FPM configuration of the present work, the tip-biprism distance,  $a \leq 1 \mu\text{m}$ , is much smaller than that between the biprism and the screen,  $b$  (16.5 cm), and the thickness of the biprism is assumed to be infinitely small. Then, the biprism equations become quite simplified. The width of the interference field,  $W$ , is given by

$$W = 2 \left| \frac{a+b}{a} \right| \left( \alpha \frac{ab}{a+b} - r \right) \approx 2\alpha b. \quad (2)$$

The electrons arriving at the same given point P on the screen would have arrived at points P1 and P2 without the biprism. The distance  $D$  between these points, termed the interference distance, is given by

$$D = 2|\alpha \cdot b| \approx W. \quad (3)$$

Eqs. (2) and (3) show that  $W$  would be equal to  $D$  for an infinitely thin filament in an FPM. In the interference region, the fringe spacing  $S$  is

$$S = \lambda \left| \frac{a+b}{2\alpha a} \right| \approx \lambda \frac{b}{2\alpha a}, \quad (4)$$

where  $\lambda$  is the wave length of the electron wave.

The performance of a biprism interferometer is enhanced with a decrease of the filament radius  $r$ , as suggested in the Eqs. (2) and (3). Carbon nanotubes are one of the thinnest but also strongest fibers in nature and are commercially available nowadays, spurring us to employ this material as the electron biprism in FPM. Pieces of multi-walled carbon nanotube (MWCNT) soot were dispersed in pure ethanol and ultrasonically agitated to unravel the bundles of tubes. A droplet of the dispersion was then deposited on the film and the film was heated inside the preparation chamber using E-Beam bombardment.

At low magnification, rather bright spots appeared near the edge of the holey carbon film in the FPM images. Using the tip approach, the magnification ratio of the shadow images increased and the bright spots evolved into equally

spaced straight fringes typical of an electron biprism interferogram. Further tip approach led to an increase of both of the number of fringes and of the width of the band of fringes, *i.e.*, the interference region. Depending on the thickness, length, *etc.*, MWCNTs generated various fringe patterns that could be categorized into three groups.

At large tip-object distances, the patterns of the first group looked rather similar to the Fresnel fringes generated by a narrow strip, simulated by Prigent *et al.*,<sup>13</sup> as shown in Figure 7(a). The tip approach changed the Fresnel-like fringe patterns into fringes of equal spacing, as shown in Figure 7(b), indicating that the MWCNT began to function as an electron biprism at small tip-object distances. A comparison of MWCNT images belonging to different groups is given in Figure 8, in which one can notice that the MWCNTs of the first group (marked by white arrows) are thicker than the MWCNTs of the other groups. This figure also shows that the MWCNTs of the first group generated only Fresnel fringes, while those of the other groups functioned as electron biprisms, revealing that the electric field around a thick tube is too weak to deflect E-Beams enough to form interference fringes at large tip-object distances.

The characteristic feature of the fringe patterns of the second group was a fan-like spreading of the interference region (marked by a white arrow), as shown in Figure 9, which also presents a straight fringe pattern belonging to the third group. The interference region widened in going from the root to the apex of an MWCNT of the second group, while the pattern of the third group exhibits nearly no spreading. Figure 10 presents a large interferogram belonging to the second group; fringe spacing near the root of the tube is larger than that near the apex. The biprism theory states that the width of the interference region  $W$  (the fringe spacing  $S$ ) is linearly (inversely) dependent on the deflection angle  $\alpha$  for an infinitely thin filament and that the angle  $\alpha$  is proportional to the intensity of the electric field.<sup>4</sup> The spreading of the interference region and the decrease of the fringe

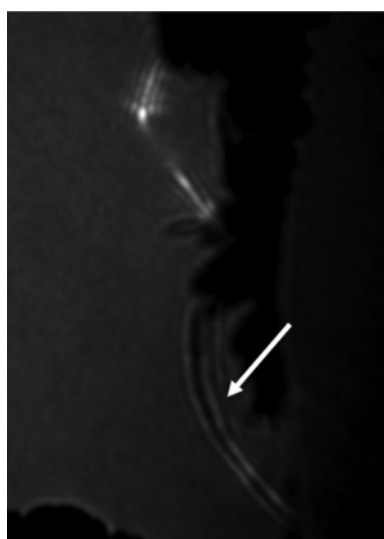


**Figure 8.** FPM image showing a nano biprism interferogram of the first group (marked by a white arrow) and the second group.

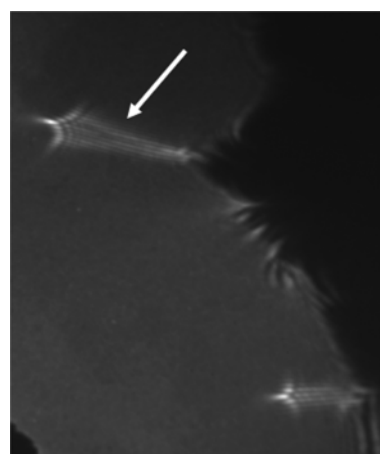


**Figure 9.** FPM image showing a nano biprism interferogram of the second group (marked by a white arrow) and the third group.

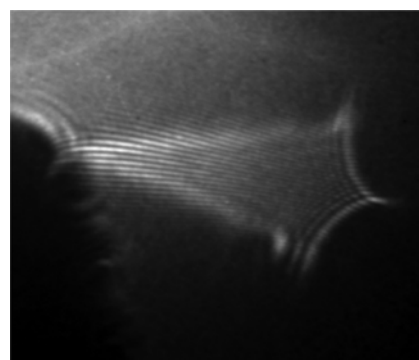


**Figure 10.** A nano biprism interferogram of the second group.

spacing thus consistently indicate that the electric field around an MWCNT increases in going from the root to the apex for the second group.

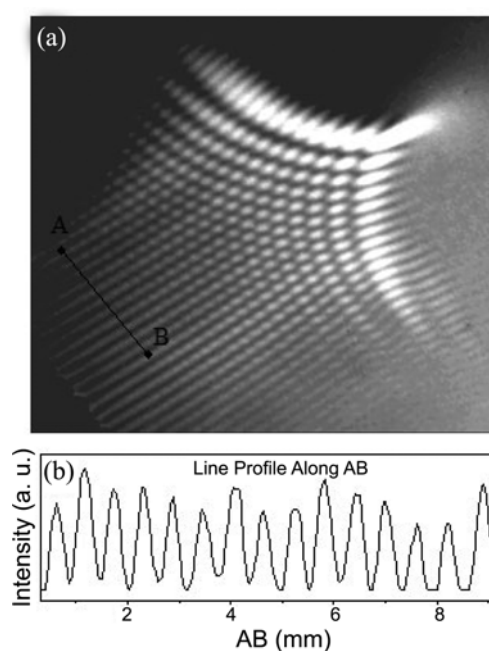


**Figure 11.** A biprism interferogram of the third group at high magnification (a) and a line profile along AB (b).

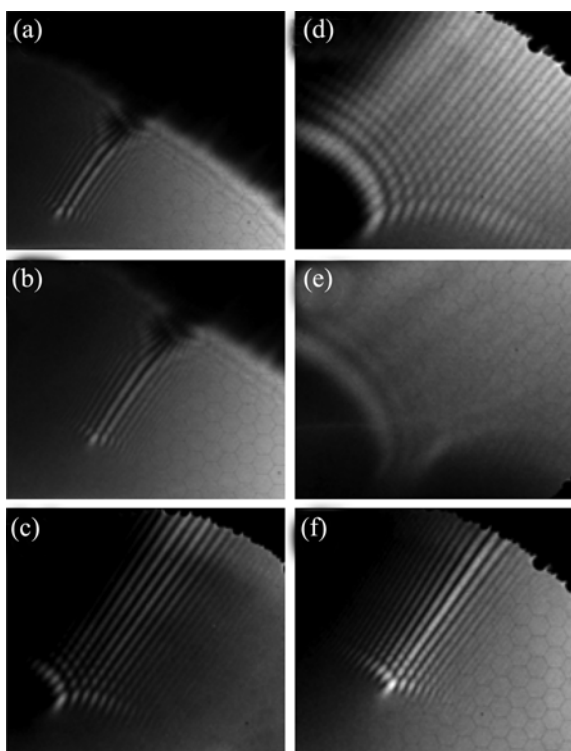


**Figure 12.** Change of a nano biprism interferogram with tip approach (a)-(c) and with tip retraction (e)-(f).

The fringe patterns of the third group generally exhibited a higher contrast compared to those of the two preceding groups, as shown in Figure 11. The line profile along the line A-B gave an average fringe spacing of 0.583 mm, with a standard deviation of 0.024 mm. The remarkable regularity of the fringe spacings demonstrated that the MWCNT functioned as an electron biprism. Figure 12 shows the evolution of a fringe pattern belonging to the third group with the variation of the tip-object distance. From the start, the fringes were of equal spacing and showed no spreading. The tip approach led to an increase of both the number of fringes and of the width of the fringe patterns. Finally, the fringe pattern became completely invisible (see Fig. 12(e)). The fringe pattern reappeared with tip retraction (see Fig. 12(f)).

The width of the interference field  $W$  increased approximately 5.5 times between Figure 12(a) and (d). Meanwhile, the fringe spacing  $S$  remained nearly the same as presented by the plot of the fringe spacing  $S$  versus the width  $W$ , as shown in Figure 13. Eq. (4) says that the fringe spacing  $S$  is proportional to the wavelength  $\lambda$  of the electron wave and inversely proportional to the tip-object distance  $a$  and the deflection angle  $\alpha$ . During the increase of  $W$ , the bias voltage changed from 130 V to 95 V, corresponding to about 17% increase of wavelength. The nearly constant fringe spacing and relatively small change of wavelength indicate that the denominator  $\alpha \cdot a$  of Eq. (4) also remained nearly constant during the tip approach.

The magnification ratio  $M$  of the FPM image  $(b+a)/a \approx b/a$  indicates that the length  $L$  of the MWCNT image on the screen is inversely proportional to  $a$ .  $L/W$  is proportional to

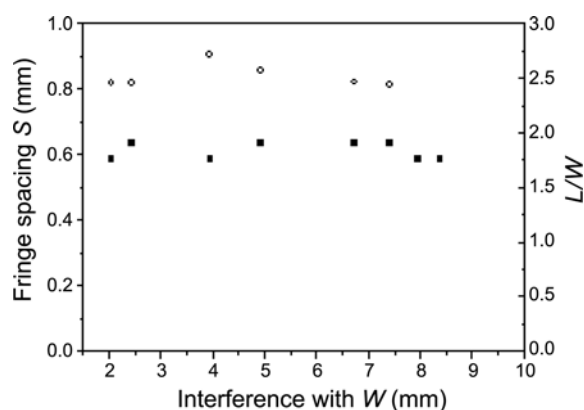


**Figure 13.** Fringe spacing  $S$  vs. width of interference field  $W$  (■) and  $L/W$  vs.  $W$  (○), where  $L$  is the length of the nanotube image on the observation screen.

$1/\alpha \cdot a$ , as is the fringe spacing  $S$ . The constancy of  $S$  then suggests that  $L/W$  would not change with tip approach, which is confirmed in the plot of  $L/W$  vs.  $W$  shown in Figure 13. The constancy of the fringe spacing  $S$  and of  $L/W$  consistently shows that  $\alpha$  is inversely proportional to  $a$ , which may reflect the fact that the electric field strength between the tip and the nanotubes increases with the decrease of tip-nanotube distance  $a$  (tip approach) and that the E-Beam deflection angle  $\alpha$  is simply proportional to the electric field strength.

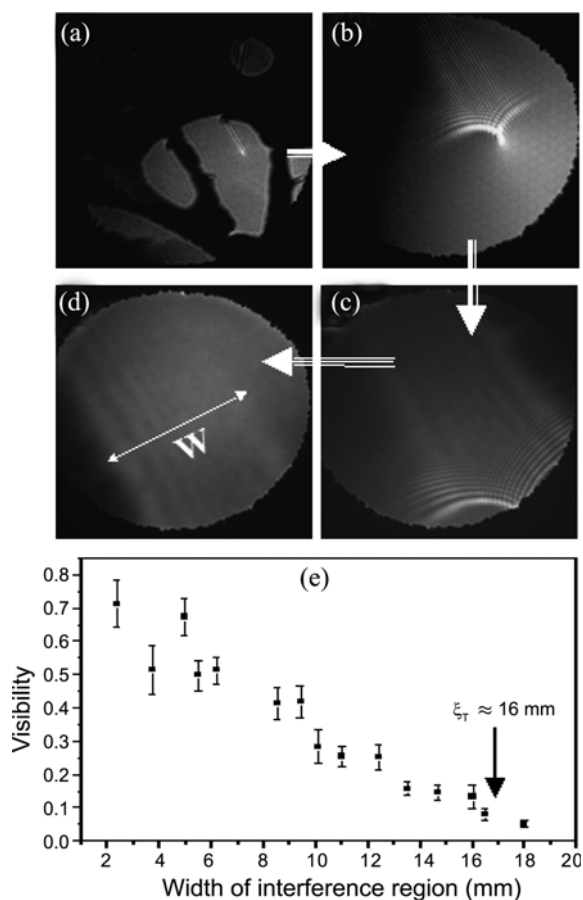
**Estimation of FE Source Coherency.** The electron biprism is one of the most widely used tools for measuring the TCL  $\xi_T$  of an E-Beam in electron microscopy.<sup>3</sup> The TCL of an E-Beam is measured by monitoring the evolution of the interference fringe visibility  $V$ , which is driven by the change of the E-Beam deflection angle  $\alpha$ . The value of  $V$  is given by

$$V \equiv \frac{I_{\max} - I_{\min}}{I_{\max} + I_{\min}}, \quad (5)$$

where  $I_{\max}$  and  $I_{\min}$  are the maximum and minimum intensity, respectively, in the fringe pattern.

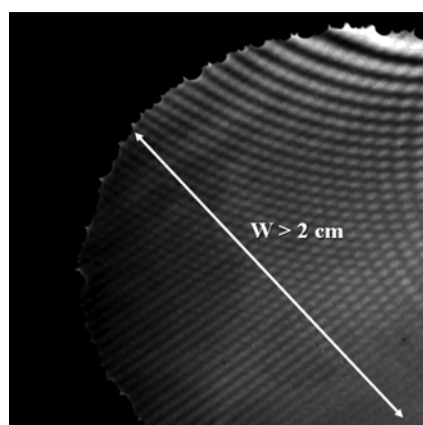
The value of  $\alpha$  increases with an increase of the positive bias voltage applied to the filament in a conventional biprism. For the electron biprism formed by MWCNTs in FPM, which we call a nano biprism in the following discussion, tip approach increases  $\alpha$ , as presented in the previous section. The width of the interference field  $W$  grows linearly with  $\alpha$ . The interference fringes are formed from the overlap of two E-Beams, which would have arrived at points on the screen separated by the interference distance  $D$  in the absence of the nano-biprism. The two beams become less coherent with an increase of  $D \approx W$ . As a result, the interference fringes blur with the increase of  $W$ , leading to the attenuation of the fringe visibility  $V$ . When the interference fringes become invisible, *i.e.*,  $V = 0$ , the measured  $W_c$  corresponds to the TCL  $\xi_T$  of an electron source on the observation screen;  $W$  ( $\approx D$ ) should be smaller than the TCL  $\xi_T$  of the beam for the generation of visible interference fringes.

Figure 14 presents a typical process for measuring the TCL  $\xi_T$ . With tip approach and consequent increase of the



**Figure 14.** Evolution of a nano biprism interferogram (a)-(d) and visibility  $V$  vs. the width of interference field  $W$  (e) with tip approach.

width of interference region  $W$ , the interference fringes continued to blur; the fringe visibility  $V$  decreased and the biprism interference fringes became invisible at  $W_c \approx 1.9$  cm, which corresponds to the TCL  $\xi_T$ . The van Cittert-Zernike theorem (1) yielded effective source sizes  $r_{\text{eff}}$  of  $\sim 0.4$  nm for  $\xi_T$  of 1.9 cm. In the meantime, the Fresnel edge fringe method gave much larger  $r_{\text{eff}}$  of  $\sim 1.5$  nm, as shown in Figure 5(b), although Figure 5(b) and Figure 14(d) were



**Figure 15.** An electron nano-biprism interferogram showing one of the largest transverse coherence length values.

taken at the same magnification.

In transmission electron microscopy (TEM), it is well known that the intensity of Fresnel edge fringes strongly depends on the thickness and straightness of the specimen edge.<sup>10</sup> Even under the same microscopy parameters, different widths of the band of Fresnel edge fringes are observed in TEM for edges of different materials. In the present paper, therefore, the TCL values determined only using nano biprisms are employed for further discussion.

The van Cittert-Zernike theorem says that the TCL  $\xi_T$  depends on the source size, varying from FE tip to tip. The value of  $\xi_T$  was measured for more than 10 tungsten FE tips. The measured value varied with changing of tip in the range of 1.2-2 cm, giving effective source sizes of 0.36-0.7 nm. Figure 15 shows an interferogram of one of the largest coherence length values obtained with a tip at room temperature.

The effective source size is equal to the real size of the source if the source is a fully incoherent one; however, the effective source sizes determined from measured transverse coherence length values (0.36-0.7 nm) were too small to be real sizes; presumably, the FE-emitters were partially coherent sources. The ratio  $K$  of the beam radius  $l_R$  and TCL  $\xi_T$  was theoretically and experimentally proved to be constant in electron microscopy by Pozzi *et al.*<sup>14,15</sup> If a typical value of  $30^\circ$  was taken for the beam-opening angle, the beam radius on the screen was  $\sim 10$  cm and the ratio  $K$  was 0.12-0.2 for the measured TCL  $\xi_T$  of 1.2-2 cm. Under the assumption that the ratio  $K$  was also constant in FPM, the coherence length on the surface of the observed field emitter was estimated to be 5-10 nm for a typical source size value of 50 nm. This finiteness of the coherence lengths on the surface of the FE emitters was in reasonable agreement with the observations of FE-patterns from MWCNT:<sup>16</sup> electrons from different sites of an MWCNT at room temperature, which are a few nm apart, can interfere with each other on the screen, showing that the coherence length on the MWCNT

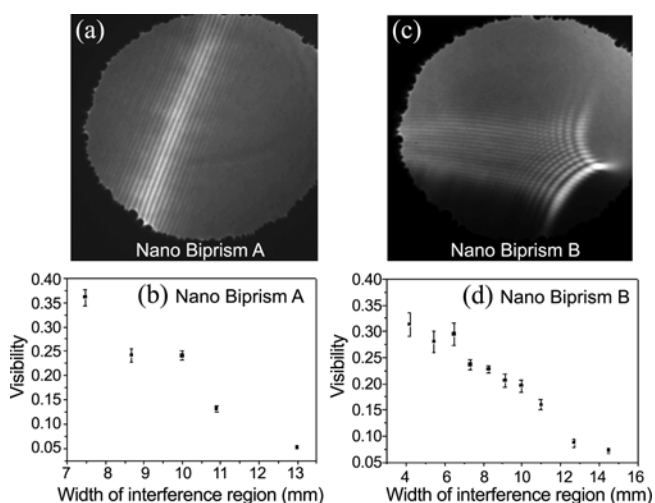


**Figure 16.** Nano biprism interferograms obtained with two different nano-biprisms (a) and (c). The visibility plots (b) and (d) show nearly the same transverse coherence length of  $\sim 13$  mm.

is a few nm.

If the TCL  $\xi_T$  is determined by the electron coherence length on the FE-emitter, the TCL  $\xi_T$  should not vary with an exchange of the nano-biprism if the same FE-emitter is used. Figure 16 compares the visibility curves of two nano-biprisms whose interferograms were obtained with the same FE-emitter. Two interferograms yield nearly the same TCL  $\xi_T$  of 13 nm on the screen.

### Conclusion

Various interferograms observed in FPM were studied in the pursuit of developing electron interferometry and holography for determining the atomic and chemical-bonding structure of molecules. The coherency of an E-Beam emitted from tungsten tips was evaluated using MWCNTs as the nano biprism. Calculated on the basis of the conductivity, the enhancement of the coherence at low temperatures agreed quantitatively with the increase in the inelastic mean free path,  $\xi_{in}$ , in solids.<sup>17,18</sup> This highly coherent E-Beam will supply a test ground for various quantum mechanical phenomena, such as the Aharonov-Bohm effect,<sup>1</sup> the anti-correlation of electron waves in vacuum,<sup>19</sup> etc.

**Acknowledgments.** This work was partly supported by Research for the Future (RFTF) in the Japan Society for the Promotion of Science. This research was partly supported by the Nano Material Technology Development Program through the National Research Foundation of Korea (NRF), funded by the Ministry of Education, Science and Technology (Grant number: 20120009639).

### References

1. Tonomura, A. *Rev. Mod. Phys.* **1987**, *59*, 639.
2. Spence J. C. H. *Experimental High-Resolution Electron Microscopy*; Oxford University Press: 1988.
3. Garcia, N.; Rohrer, H. *J. Phys.: Condens. Matter* **1989**, *1*, 3737.
4. Missiroli, G. F.; Pozzi, G.; Valdre, U. *J. Phys. E* **1999**, *14*, 649.
5. Born, M.; Wolf, E. *Principles of Optics*, 7th ed.; Cambridge University Press.
6. Fink, H. W.; Schmid, H.; Kreuzer, H. J.; Wierzbicki, A. *Phys. Rev. Lett.* **1991**, *67*, 1543.
7. Spence, J. C. H.; Qian, W.; Silverman, M. P. *J. Vac. Technol. A* **1994**, *12*, 542.
8. Fransen, M. J.; Damen, E. P. N.; Schiller, C.; van Rooy, T. L.; Groen, H. B.; Kruit, P. *App. Surf. Sci.* **1996**, *94/95*, 107.
9. de Jonge, N.; Lamy, Y.; Schoots, K.; Oosterkamp, T. H. *Nature* **2002**, *420*, 393.
10. Horiuchi, S. *Fundamentals of High-resolution Transmission Electron Microscopy*; Amsterdam: North-Holland, 1994.
11. Cho, B.; Ichimura, T.; Shimizu, R.; Oshima, C. *Phys. Rev. Lett.* **2004**, *92*, 246103.
12. Cho, B.; Ogawa, T.; Ichimura, T.; Ichinokawa, T.; Amakusa, T.; Oshima, C. *Rev. Sci. Instrum.* **2004**, *75*, 3091.
13. Prigent, M.; Morin, P. *J. Microscopy* **2000**, *199*, 197.
14. Pozzi, G. *Optik* **1987**, *77*, 69.
15. Pozzi, G.; Matteucci, G.; Carpenter, R. W. *Eleventh International Congress on Electron Microscopy*, Kyoto **1984**, *1*, 315.
16. Oshima, C.; Mastuda, K.; Kona, T.; Mogami, Y.; Komaki, M.; Murata, Y.; Yamashita, M.; Kuzumaki, T.; Horiike, Y. *Phys. Rev. Lett.* **2002**, *88*, 38301.
17. Meaden, G. T. *Electrical Resistance of Metals*; Heywood Books, London, 1966.
18. Jeandupeux, O.; Burgi, L.; Hirstein, A.; Brune, H.; Kern, K. *Phys. Rev. B* **1999**, *59*, 15926.
19. Kiesel, H.; Renz, A.; Hasselbach, F. *Nature* **2002**, *418*, 392.